


 Cite this: *RSC Adv.*, 2022, **12**, 26134

Low Au-content CoAu electrodes for environmental applications†

Kristina Radinović, ^a Jadranka Milikić, ^a Aldona Balčiūnaitė, ^b Zita Sukackienė, ^b Marko Bošković, ^c Loreta Tamašauskaitė-Tamašiūnaitė ^b and Biljana Šljukić ^{*ad}

Six cobalt gold (CoAu) electrodes were prepared by electroless deposition using different gold-containing solutions (acidic and weakly acidic) and different Au deposition times. Characterization of CoAu electrodes was done by scanning electron microscopy with energy-dispersive X-ray spectroscopy, N₂-sorption, and X-ray powder diffraction techniques. The possibility of using the prepared electrodes in environmental applications, *i.e.*, for the electrochemical sensing of a trace amount of arsenic(III) in weakly alkaline media was assessed. Employing the CoAu electrode (prepared by immersing Co/Cu into 1 mM HAuCl₄ (pH 1.8) at 30 °C for 30 s) under optimized conditions (deposition potential –0.7 V and deposition time of 60 s), a low limit of detection of 2.16 ppb was obtained. Finally, this CoAu electrode showed activity for arsenic oxidation in the presence of Cu(II) as a model interferent as well as in real samples. Furthermore, the use of CoAu electrode as an anode in fuel cells, namely, direct borohydride – hydrogen peroxide fuel cells was also assessed. A peak power density of 191 mW cm⁻² was attained at 25 °C for DBHPFC with CoAu anode at a current density of 201 mA cm⁻² and cell voltage of 0.95 V, respectively. The peak power density further increased with the increase of the operating temperature to 55 °C.

Received 2nd August 2022
 Accepted 6th September 2022

DOI: 10.1039/d2ra04828k
rsc.li/rsc-advances

1. Introduction

Environmental safety and human health protection have become the primary goals in the present day. Namely, rapid economic development along with many benefits has also brought problems of environmental pollution and the depletion of fossil fuels that are currently the main energy sources. To overcome these challenging issues, research has been devoted to the development of clean and renewable energy sources along with sensors to monitor the level of environmental pollution. Among different types of novel energy technologies and sensors, electrochemical energy conversion devices and electrochemical sensors have been pointed out as especially promising.

To operate with high efficiency and selectivity, these devices typically need to employ highly active electrocatalysts. Gold

(Au)-based materials are seen as promising for various electrocatalytic reactions due to their high catalytic activity and selectivity.¹ Au-based nanomaterials can be prepared by different methods that will further determine their composition, morphology, and particle size, and consequently, their electrochemical response. Within the present paper, we report a simple and fast electroless deposition procedure for the preparation of CoAu electrodes and we next focus on the use of the prepared CoAu electrodes for electrochemical sensing (with arsenic(III) as model analyte) and for electrocatalytic applications in fuel cells (namely, for borohydride oxidation reaction (BOR)). Au metal has demonstrated high activity for the electrochemical sensing of trace amounts of As(III),² as well as high activity for BOR along with low activity for parasitic borohydride (BH₄⁻) hydrolysis reaction (more details below).³ Non-noble metals such as Co have been investigated for instance, for BOR;⁴ however, they typically show more pronounced activity for a hydrolysis reaction.⁵ Thus, we aim to keeping the high efficiency of Au-based electrodes but notably lowering the price of the electrode material.

Arsenic (As), a model analyte tested herein, is undoubtedly one the most toxic ions in the group of heavy metal ions^{6,7} and it exists both naturally and in industrial effluents.^{8–12} Dominant forms of inorganic arsenic species in natural water are As(III) (AsO₃³⁻) and As(V) (AsO₄³⁻)^{8–12} with the former being about 60–70 times more toxic than As(V). The World Health Organization has limited the maximum concentration of arsenic in natural water to as low as 10 ppb.^{6,12–14} Therefore, fast and accurate

^aUniversity of Belgrade, Faculty of Physical Chemistry, Studentski trg 12-16, Belgrade 11158, Serbia

^bCenter for Physical Sciences and Technology, Saulėtekio ave. 3, Vilnius LT-10257, Lithuania

^cUniversity of Belgrade, Institute of Chemistry, Technology, and Metallurgy, Department of Microelectronic Technologies, Njegoševa 12, Belgrade 11000, Serbia

^dCenter of Physics and Engineering of Advanced Materials, Laboratory for Physics of Materials and Emerging Technologies, Chemical Engineering Department, Instituto Superior Técnico, Universidade de Lisboa, Lisbon 1049-001, Portugal. E-mail: biljka@ffh.bg.ac.rs

† Electronic supplementary information (ESI) available. See <https://doi.org/10.1039/d2ra04828k>

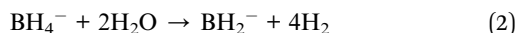


detection of As(III) in the environment is particularly significant. Various analytical methods, such as atomic flame absorption spectrophotometry, hydride-generation atomic absorption, emission spectrometry, inductively coupled plasma optical emission spectrometry, and inductively coupled plasma mass spectrometry have been traditionally used for the detection of heavy metals.⁷ However, these instrumental methods require specialised laboratory conditions and lengthy sample preparation. On the other hand, electrochemical methods are highly selective, and fast and require cheaper and portable equipment suitable for field analysis.^{15,16} Different types of Au-based electrodes were tested as arsenic sensors in aqueous media. Three-dimensional porous graphitic carbon nitride decorated by Au nanoparticles (AuNPs/g-C₃N₄) gave a response in the presence of As(III) species in different real samples, including tap water, spring water from the mountain, and the water from the river.² Alloys of Au and Rare Earth (RE) elements showed good performance for the electroanalytical determination of As(III) in weakly alkaline media. The limit of detection (LOD) of As(III) obtained with the tested alloys was far below the WHO value and increased in the order: Au–Ho (0.8 ppb) < Au–Dy (1.5 ppb) < Au–Y (1.6 ppb) < Au–Sm (2.3 ppb).⁶ Gold–copper (Au–Cu) bimetallic nanoparticles prepared by the hydrothermal method presented high performance as arsenic sensors with high sensitivity at ppb level where Au₈₉Cu₁₁ electrodes with the highest content of Cu showed the best stripping behaviour and the highest sensitivity for As(III) detection.¹⁷ Electrodes based on cobalt oxide nanoparticles (CoO_x) showed to be excellent arsenic sensors at a wide pH range from 5 to 11¹⁸ displaying a clear peak corresponding to arsenic oxidation.

As mentioned, another important aspect of preserving environmental safety is the reduction of greenhouse gases emission from the combustion of fossil fuels. Thus, energy needs to be generated using clean energy sources such as fuel cells. The direct borohydride fuel cells, which use an aqueous solution of borohydride (NaBH₄) as a fuel and oxygen (DBFCs) or hydrogen peroxide (DBHPFCs) as the oxidant, are considered to have great energy potential and high energy density.¹⁹ The reaction taking place at the DBFC anode, BOR, can involve a maximum of eight electrons, according to eqn (1):^{20,21}



It is known that in practice it is difficult to achieve the transfer of eight electrons due to the parallel hydrolysis of BH₄[–] (eqn (2)), a spontaneous reaction that consumes part of the BH₄[–] ions present in the solution and generates hydrogen.²²



Au typically has a lower activity for hydrolysis reaction,²³ so it can lead to the indicated number of exchanged electrons.^{24–26} The disadvantage is the slow BOR kinetics on the Au anode, which leads to low power output and poor electrochemical performance of DBFCs.²⁷ Studies have shown that alloying Au with lower-cost metals can improve catalytic performance and, at the same time, reduce the cost of the material. Promising

results have been obtained for a variety of non-noble metals, such as Co, Ni, Cu, Zn, and Fe.²⁸ Pei *et al.* reported that supported Au–Co alloy catalysts have higher catalytic activity for the direct oxidation of BH₄[–] than pure nano-sized Au catalyst, especially the Au₄₅Co₅₅/C catalyst.²⁹ Catalytic activity for BOR of a series of electrocatalysts based on Au modified with Zn was reported to be higher than in the case of a pure Au electrode.³⁰ Au–RE: Au–Sm, Au–Dy, Au–Ho, and Au–Y, alloys tested for BOR showed significantly higher current densities compared to the Au electrode for BOR.²⁸

Thus, as mentioned, we herein present an easy synthesis of CoAu electrodes by simple electroless deposition and characterise them using scanning electron microscopy/energy dispersive X-ray spectroscopy (SEM-EDS), N₂-sorption and X-ray diffraction (XRD) techniques. The anodic stripping voltammetry (ASV) method was used for As(III) detection while cyclic voltammetry and chronoamperometry were used for the BOR studies.

2. Experimental

2.1. Reagents and materials

A stock solution of As(III) (1 mM) was prepared by dissolving 3.25 mg of sodium arsenite (NaAsO₂, Fisher Chemical) in 25 cm³ of deionized water (Simplicity® UV Water Purification System, Merck Millipore). Sodium hydrogen carbonate (NaHCO₃, Zdravljke Leskovac) and sodium carbonate anhydride (Na₂CO₃, Zorka Šabac) were used for the preparation of NaHCO₃ + Na₂CO₃ buffer. Copper sulfate (CuSO₄, NRK Engineering Belgrade) was used for studying the influence of interferences on the electrode's response to As(III). Sodium borohydride (NaBH₄, Scharlau, 97 wt%) and sodium hydroxide (NaOH, Sigma-Aldrich) were used for the preparation of anolyte, while H₂O₂ (30 vol%, Carlo Erba) and HCl (37 wt%, Sigma Aldrich) were used for the preparation of catholyte. All solutions were prepared using deionized water (Simplicity® UV Water Purification System, Merck Millipore).

2.2. Preparation of gold cobalt electrodes

Electroless deposition of Co was performed on the copper surface with a prior activation step with Pd(II) ions. Briefly, prior to electroless deposition of Co, Cu sheets (1 cm × 1 cm) were pre-treated with 50–100% calcium magnesium oxide, known as “Vienna Lime” (Kremer Pigments GmbH & Co. KG), and rinsed with deionized water. Then the Cu sheets were placed into the electroless cobalt bath containing 0.05 M CoSO₄, 0.05 M C₄H₈ONH, BH₃ and 0.2 M glycine (NH₂CH₂COOH). The bath operated at pH 7 at a temperature of 30 °C for 30 min. The temperature of 30 °C was observed to be the optimum one for the deposition of these coatings. At a lower temperature, the coatings were applied unevenly and not smoothly. At a higher temperature, the adhesion became worse and the coatings started to “crumble” and to have some cracks. The thickness of the pure Co coatings determined gravimetrically was *ca.* 1 µm.^{31,32} Transmission electron microscopy (TEM) analysis of the deposited Co coating was carried out using FEI TECNAI F20 field emission microscope operating at 200 kV.

Au nanoparticles were deposited on the prepared Co/Cu electrodes by galvanic displacement of Au at a temperature of 30 °C from a 1 mM HAuCl₄ solution (pH 1.8) (denoted as an acidic Au-containing solution) or from a 1 g l⁻¹ KAu(CN)₂ + 0.4 M (NH₄)₂C₆H₆O₇ complex (pH 5) (denoted as a weak acid Au-containing solution).

The immersion periods of the Co/Cu electrodes into the gold-containing solutions were 0.5, 1, and 5 min. After plating, the samples were taken out, thoroughly rinsed with deionized water, and dried in air at room temperature.

2.3. Characterization of CoAu electrodes

XRD analysis (with X-ray diffractometer D2 Phaser Bruker AXS) and SEM-EDX (with scanning electron microscope TM4000Plus Hitachi) were conducted to provide comprehensive information about the structure and dispersion of active components on the surface of the electrodes prepared. XRD patterns were recorded using Cu K α radiation. A step-scan mode was used in the 2 θ range from 30° to 90° with a step length of 0.04° and a counting time of 1 s per step. Sorption isotherm of CoAu (30 s, pH 1.8) was obtained by nitrogen sorption at 77 K using a Quantachrome Instruments NOVA touch 2LX device. Prior to adsorption, the sample was degassed for 15 min at 80.0 °C, then 30 min at 120.0 °C, and finally for 180 min at 300.0 °C. The specific surface area of the sample, S_{BET} , was calculated using the multi-point Brunauer–Emmett–Teller (BET) method.

2.4. DFT calculation studies

PWscf code³³ of Quantum espresso program package was used for all the spin-polarized DFT calculations, within generalized gradient approximation (GGA) using the PBE³⁴ functional formulation. Projector augmented wave (PAW) pseudopotentials were employed to describe the interactions between ionic cores and valence electrons.³⁵ The valence electronic states were expanded in plane-wave basis sets with a cutoff energy of 35 Ry (476 eV). The adsorption energy was calculated as $E_{\text{ads}} = E_{\text{mol/surf}} - (E_{\text{surf}} + E_{\text{mol}})$, where E_{mol} , E_{surf} , and $E_{\text{mol/surf}}$ are the total energy of H₃AsO₃ molecules/Arsenic atoms, and gold/cobalt layer without and with H₃AsO₃ molecules/Arsenic atoms. A larger negative E_{ads} value means a more stable configuration.

2.5. Electrochemical measurements

2.5.1 Arsenic(III) sensing. The As(III) electroanalytical sensing investigations were performed using PalmSense EmStat3 Blue Potentiostat within a glass cell of 25 ml volume with a standard three-electrode system. A carbon graphite rod and saturated calomel electrode (SCE) were employed as counter and reference electrodes, respectively. Thus, all potentials in this work are given *vs.* SCE reference. NaHCO₃ + Na₂CO₃ buffer (pH 9.2–10.6) was used as supporting electrolytes for all electrochemical measurements related to As(III) detection. Alkaline media was used due to the possible instability of CoAu electrodes in acidic media. All As(III) sensing studies were conducted at room temperature under a nitrogen (N₂, Messer) atmosphere.

The electrochemical characterization of CoAu electrode was performed by cyclic voltammetry (CV) in NaHCO₃ + Na₂CO₃

buffer (pH in the 9.2–10.6 range). An area of 1 cm² of CoAu working electrode was exposed to the electrolyte and used for calculating current densities.

Electroanalysis of As(III) presence was investigated by anodic stripping voltammetry (ASV)³¹ with optimization of the working parameters: scan rate, deposition potential, E_{d} , and deposition time, t_{d} . The impact of different E_{d} (−0.3 to −0.9 V) and t_{d} (30 to 360 s) on As(III) oxidation was examined.

For comparison purposes, a pure Au electrode with a geometric area of 0.19625 cm², was also tested.

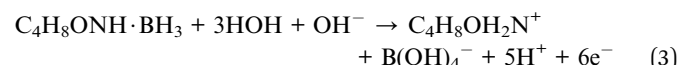
The real water samples from the river Danube and river Begej were diluted with NaHCO₃ + Na₂CO₃ buffer (sample: buffer 75 : 25 vol% ratio).

2.5.2 Borohydride oxidation reaction study. Initial studies of Co and CoAu electrodes' activity for BOR were carried out by cyclic voltammetry and chronoamperometry in 0.05 M NaBH₄ + 1 M NaOH at 25 °C. DBHPFC tests were carried out by employing the Co and CoAu electrodes with a geometric area of 2 cm² as the anode and a Pt sheet as the cathode. The catholyte was composed of an alkaline mixture of 1 M NaBH₄ + 4 M NaOH and the anolyte contained 5 M H₂O₂ + 1.5 M HCl. Each compartment of the cell contained 100 ml of the corresponding aqueous electrolyte. In order to prevent H₂O₂ decomposition and possible loss of BH₄[−] by hydrolysis during storage, the test solutions were prepared immediately before the measurements. A Nafion N117 membrane was used to separate the anodic and cathodic compartments of the single direct NaBH₄/H₂O₂ fuel cell. The presented current densities are normalized with respect to the geometric area of electrodes. All electrochemical measurements were performed with a Zennium electrochemical workstation (ZAHNER-Elektrik GmbH & Co. KG). The performance of the fuel cell was evaluated by recording the cell polarization curves and constructing the corresponding power density curves.

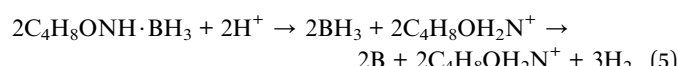
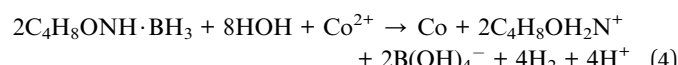
3. Results and discussion

3.1. Characterization

The initial stage of Co deposition on the substrate, anodic oxidation of morpholine borane (C₄H₈ONH·BH₃, MB), can be presented as follows (eqn (3)) (Scheme 1):



The electrons released within this reaction are consumed for the reduction of cobalt(II) ions (eqn (4)) and boron (eqn (5)):



At the same time, some quantity of morpholine borane may be additionally consumed in the following reaction (eqn (6)):



Fig. S1† shows TEM image of the cross section of Co deposited onto Cu under conditions described in the Experimental section. The rate of Co deposition and the composition of the Co coatings were observed to depend on the solution pH and MB concentration.³⁶ Increase of pH (from 6 to 8) accelerates the rate of Co reduction most likely due to the acceleration action of OH⁻ ions to the first step of the process – morpholine borane anodic oxidation (eqn (3)). Furthermore, increase of pH led to a lower amount of boron incorporated in Co coatings.

With the increase in morpholine borane concentration in the solution, its anodic oxidation accelerated and, consequently, the Co deposition rate increased markedly as well. This rise in Co deposition rate with increase in concentration of MB in the solution was also reflected in the changes in the composition of the coatings, *i.e.*, in the decrease of the quantity of Co in coatings.

The immersion deposition of Au particles is a galvanic replacement reaction. Namely, due to the difference between standard potentials of the Co²⁺/Co and Au³⁺/Au pairs (eqn (7) and (8), respectively), the reaction (eqn (9)) takes place:

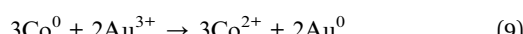
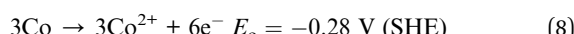
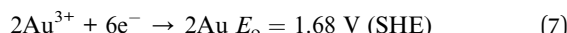


Fig. 1a and b presents SEM images of CoAu (30 s, pH 1.8) electrode at different magnifications where Au nanoparticles visible as bright crystallites of mostly round shape are evenly distributed over the entire surface of the Co-coated electrode. SEM-EDS mapping of the surface of CoAu (30 s, pH 1.8) electrode (Fig. 1c) shows the element distribution where Co and Au nanoparticles are homogeneously dispersed on the copper surface.

Amounts of metals deposited on the CoAu (30 s, pH 1.8) electrode surface were determined by EDS and found to be 96.41 and 3.59 wt% for Co and Au, respectively (Table 1).

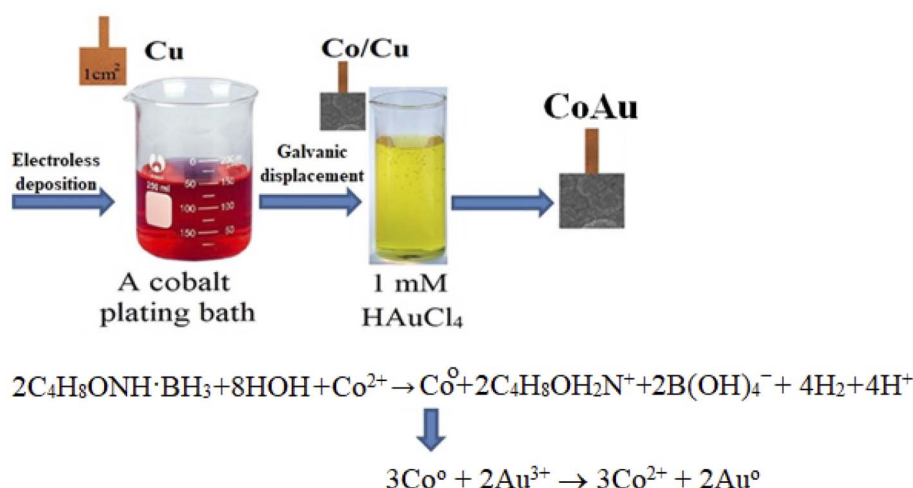
Specific surface area of CoAu (30 s, pH 1.8) according to the BET isotherm, S_{BET} , was found to be 30 m² g⁻¹.

Additional structural characterization of CoAu (30 s, pH 1.8) electrode was done by XRD analysis (Fig. 2). The reflections from Co(111) and Co(101) planes were observed at 2θ of 44.4 and 50.1°, respectively.³⁷ The low-intensity peaks at 2θ of 37.9 and 46.5° originate from the reflections from Au(111) and Au(200) crystalline planes, respectively.³ The highest intensity peak at 2θ of 73.9° and a lower intensity peak at 2θ of 43.1° correspond to the reflection from Cu(220) and Cu(111) planes of Cu substrate, respectively.^{38,39}

The electrochemical characterization of CoAu (30 s, pH 1.8) electrode in NaHCO₃ + Na₂CO₃ buffer (Fig. 3a) shows the oxidation of Au at *ca.* 0.6 V with a corresponding reduction peak at *ca.* 0.4 V on the reverse scan.⁴⁰

3.2. As(III) sensing using CoAu electrode

Two sets of CoAu electrodes were tested for electroanalytical detection of As(III) in a weakly alkaline medium (NaHCO₃ + Na₂CO₃ buffer). The first set of electrodes was prepared by immersing Co/Cu into 1 mM HAuCl₄ (pH 1.8) at 30 °C for different periods (30 s, 60 s, and 300 s) and all three prepared electrodes were active for detection of As(III). The activity for As(III) sensing was evidenced by the appearance of an oxidation peak in the voltammograms; Fig. S2a† illustrates the case of electrode prepared by immersion during 30 s. However, the electrodes prepared with 60 s and 300 s became passive after some time as evidenced by the disappearance of the previously observed oxidation peak, Fig. S2b and c.† The second set of electrodes was prepared by immersing Co/Cu into 1 g l⁻¹ KAu(CN)₂ + 0.4 M (NH₄)₂C₆H₆O₇ complex (pH = 5) at 30 °C for various periods (30 s, 60 s, and 300 s) and all prepared electrodes were inactive for As(III) detection. Namely, no peak



Scheme 1 Schematic representation of material synthesis by electroless deposition.



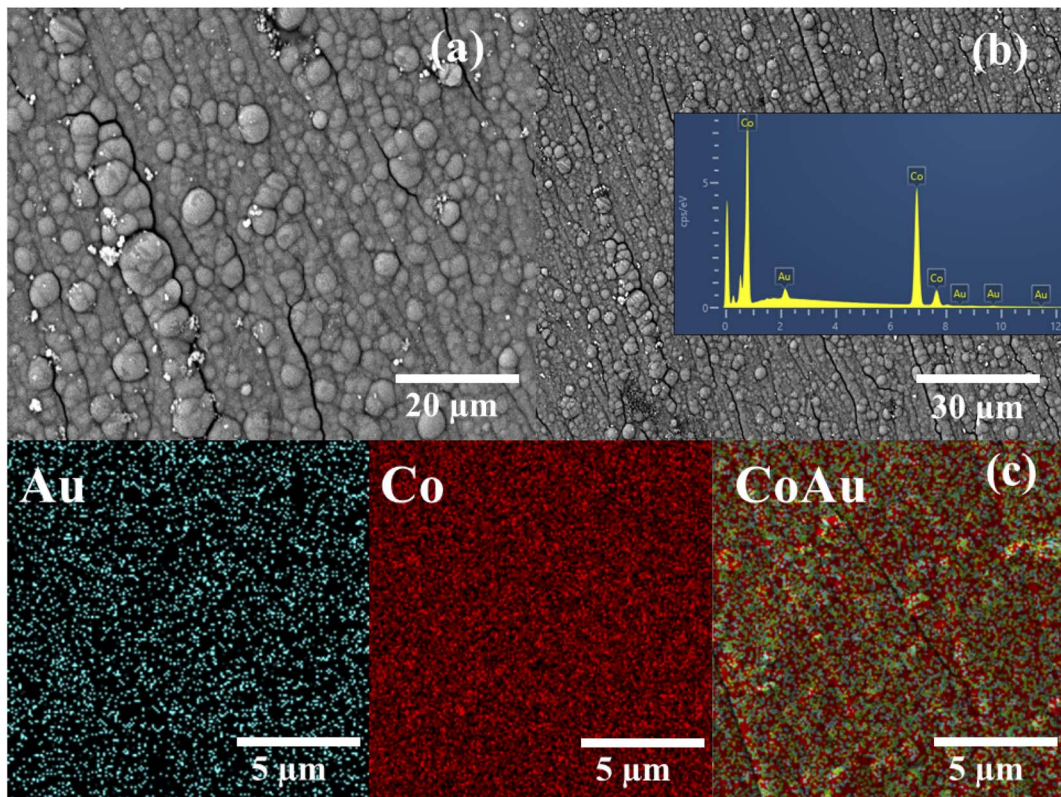


Fig. 1 (a and b) SEM images of CoAu (30 s, pH 1.8) at different magnifications with EDS spectrum (inset) and (c) SEM-EDS mapping of CoAu (30 s, pH 1.8) electrode.

Table 1 Surface weight (%) and atomic composition (%) of the CoAu (30 s, pH 1.8) electrode determined by EDS analysis

Whole surface		
	Weight (%)	Atomic (%)
Co	96.41	98.90
Au	3.59	1.10

corresponding to As oxidation was observed when using such fabricated CoAu electrodes, Fig. S2d, e and f.† Therefore, the CoAu (30 s, pH 1.8) electrode prepared by immersing Co/Cu into 1 mM HAuCl₄ (pH 1.8) for 30 s was examined in detail (and it is from this point onward refereed in the text just as CoAu electrode).

Voltammogram of CoAu electrode in the presence of As(III) showed a clear peak of As(0) oxidation to As(III), Fig. 3b. As(0) oxidation at the potential of *ca.* -0.36 V was also reported when testing As(III) sensing using Au-RE (RE = Sm, Ho, Dy, Y) electrodes in the same buffer.⁶ The oxidation peak reached a current density of 0.20 mA cm⁻² (current density difference in the presence and in the absence of As(III) at -0.36 V). Fig. 3c illustrates the behaviour of a bulk Au electrode that gave *ca.* 8.5 times lower peak current density in the presence of As(III) relative to the CoAu electrode.⁴¹

It is known that the determination of As(III) using ASV involves two steps:⁴² during the first step, As(III) is reduced to

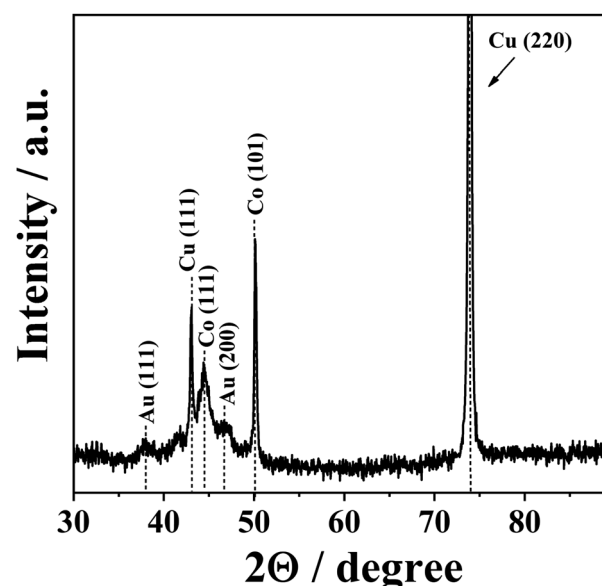
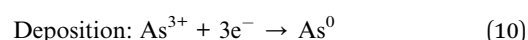


Fig. 2 XRD pattern of CoAu (30 s, pH 1.8) electrode.

As(0) and adsorbed on the electrode surface (eqn (10)); then the adsorbed As (0) is removed from the electrode surface back to the solution by oxidation to As(III) (eqn (11)) (Scheme 2).^{7,18,35}



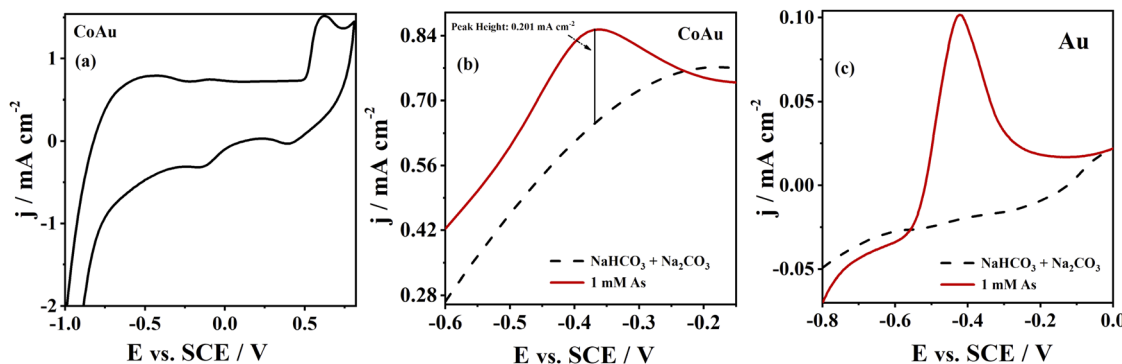
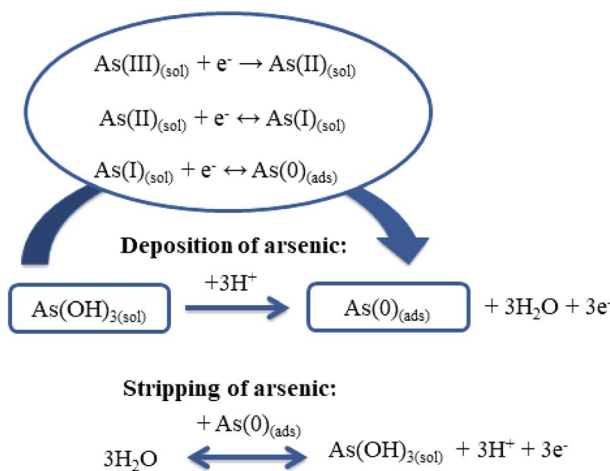
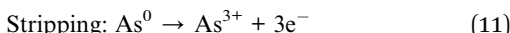


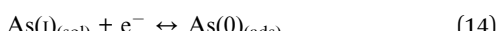
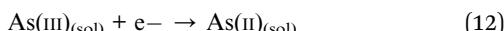
Fig. 3 (a) CV of CoAu electrode in $\text{NaHCO}_3 + \text{Na}_2\text{CO}_3$ buffer, ASV of (b) CoAu electrode, and (c) bulk Au electrode in $\text{NaHCO}_3 + \text{Na}_2\text{CO}_3$ buffer in the absence and in the presence of As(III) (1 mM) recorded at a scan rate of 50 mV s^{-1} after holding the potential at -0.7 V for 60 s.



Scheme 2 Schematic representation of the electroanalytical sensing of As(III).



Theoretical considerations of the mechanism of As(III) deposition (eqn (12)–(14)) have indicated transfer of the first electron as the rate-determining step:⁷



In order to gain insight into the adsorption process, the adsorption energy of arsenic acid and atomic arsenic on the planes of gold(111) and (200) and on the planes of cobalt(111) and (101) were calculated, Table 2. The adsorption energies of arsenic acid correspond to chemisorption, while the energy in the case of arsenic atoms corresponds to the formation of a metal layer on the surfaces.

The effect of the scan rate on the arsenic oxidation at CoAu electrode in $\text{NaHCO}_3 + \text{Na}_2\text{CO}_3$ buffer (Fig. 4) is demonstrated

Table 2 Results of calculation of the adsorption energy of H_3AsO_3 and As atomic

	$E_{\text{ads}}(\text{H}_3\text{AsO}_3) [\text{kJ mol}^{-1}]$	$E_{\text{ads}}(\text{As}) [\text{kJ mol}^{-1}]$
Au(111)	-190	-1259
Au(200)	-147	-1703
Co(111)	-122	-760
Co(101)	-234	-988

as shifting of the oxidation peak to more positive potential values with increasing the scan rate. This behaviour of CoAu electrode during As(0) to As(III) oxidation is typical for an irreversible process.⁴³ Fig. 4(b and c) shows the peak current density corresponding to oxidation of As(0) to As(III) as a function of scan rate and the square root of scan rate, respectively. The coefficient of determination (R^2) of the j_p vs. $\nu^{1/2}$ plot is found to be 0.99975 indicating that diffusion of active species plays (Scheme 1) role in arsenic oxidation.⁴⁴

Furthermore, the deposition process, *i.e.*, deposition parameters (E_d and t_d), were optimised. The highest As(III) oxidation peak current density at CoAu electrode was obtained for the deposition potential of -0.9 V , decreasing at less negative potentials (Fig. 5a). Still, a deposition potential of -0.7 V was selected for further measurements to avoid subjecting the electrode to high negative potentials. The highest current density of 0.85 mA cm^{-2} of CoAu electrode was obtained at a deposition time of 60 s (Fig. 5c). Namely, the current density for a deposition time of 30 s was slightly lower (0.84 mA cm^{-2}) than for 60 s (0.85 mA cm^{-2}). Unexpectedly, the peak current density of CoAu electrode was decreased above 60 s where the lowest current density of 0.72 mA cm^{-2} was obtained for 360 s (Fig. 5d).

The standard addition plot of As(III) sensing using CoAu electrode was obtained under the optimised deposition conditions. The increase of peak current density with the increase of the As(III) concentration in the range from 2 to 20 ppb could be seen (Fig. 6a) and the corresponding peak current, i_p , vs. concentration, c , plot data (Fig. 6a[inset]) were used for determining the LOD value using the 3 sigma method.⁴⁵ Thus, LOD of As(III) sensing with CoAu electrode was found to be as low as



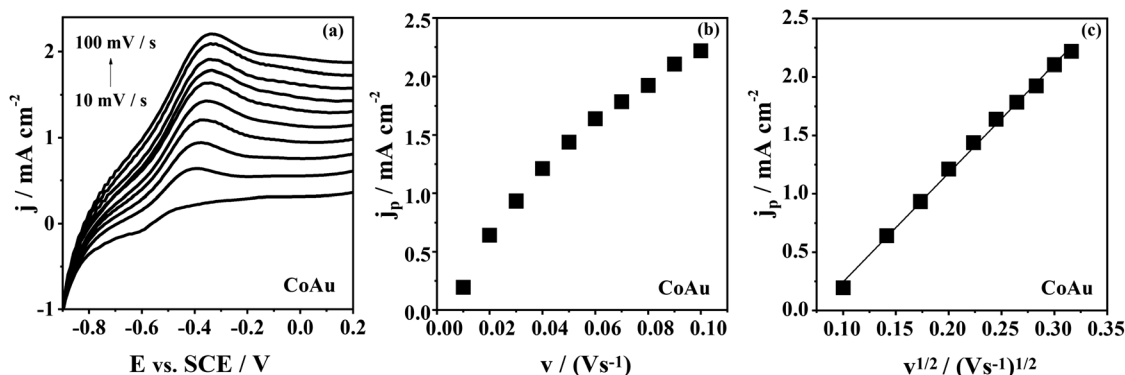


Fig. 4 (a) Voltammograms of CoAu electrode at different scan rates after holding the potential at -0.7 V for 60 s with, (b) the corresponding j_p vs. v plot of CoAu electrode, and (c) the corresponding j_p vs. $v^{1/2}$ plot of CoAu electrodes.

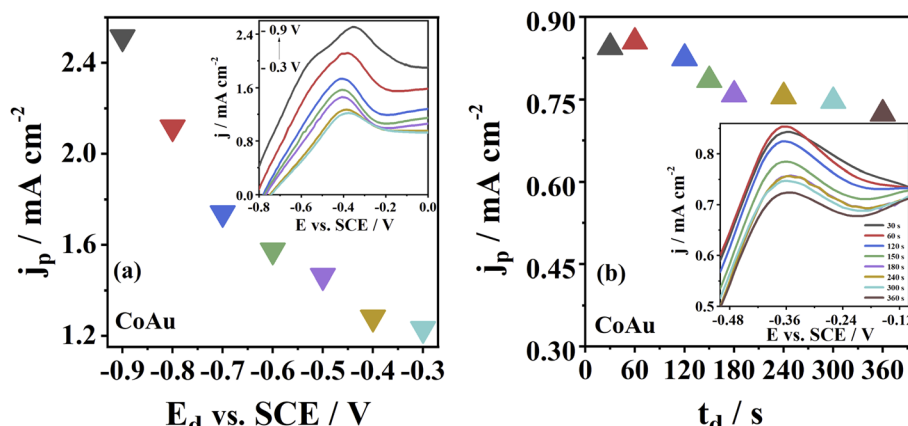


Fig. 5 (a) Voltammograms of CoAu electrode recorded using different deposition potentials, E_d , during 180 s with the corresponding j_p vs. E_d plot (inset). (b) Voltammograms of CoAu electrode recorded using different deposition times, t_d , (at -0.7 V) with the corresponding j_p vs. t_d graph (inset). All measurements were done in 1 mM As(III) in $\text{NaHCO}_3 + \text{Na}_2\text{CO}_3$ buffer at a scan rate of 50 mV s $^{-1}$.

2.16 ppb. The obtained value is well below the maximum allowed As concentration (10 ppb) in drinking water set by WHO⁴⁶ suggesting that the herein-tested CoAu electrode could

be a good electrode material for As(III) sensing. Further, this value is lower than the LOD of 25.98 ppb obtained with the glassy carbon electrode (GCE) modified with nano Au-crystal

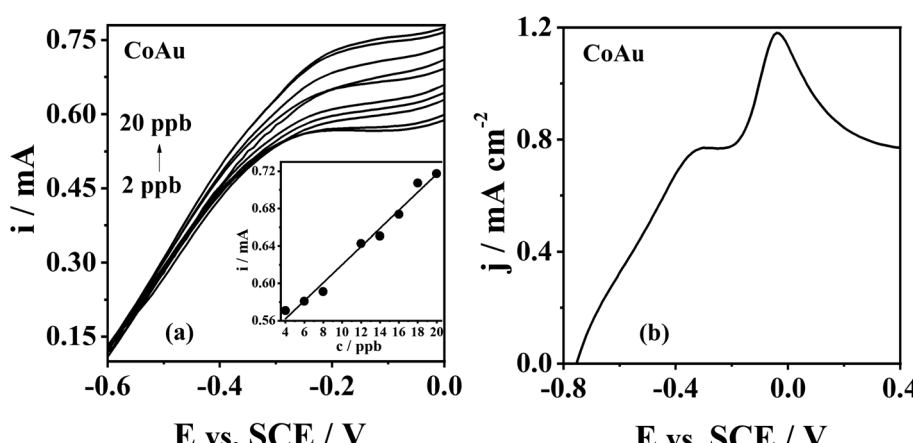


Fig. 6 (a) Voltammograms of CoAu electrode in $\text{NaHCO}_3 + \text{Na}_2\text{CO}_3$ buffer with increasing concentrations of As(III) (2 to 20 ppb) with the corresponding standard addition plots (inset). (b) Voltammogram of CoAu electrode in As (1 mM) + Cu (1 mM) solution in $\text{NaHCO}_3 + \text{Na}_2\text{CO}_3$ buffer. Voltammograms recorded at a scan rate of 50 mV s $^{-1}$ after holding the potential at -0.7 V for 60 s.



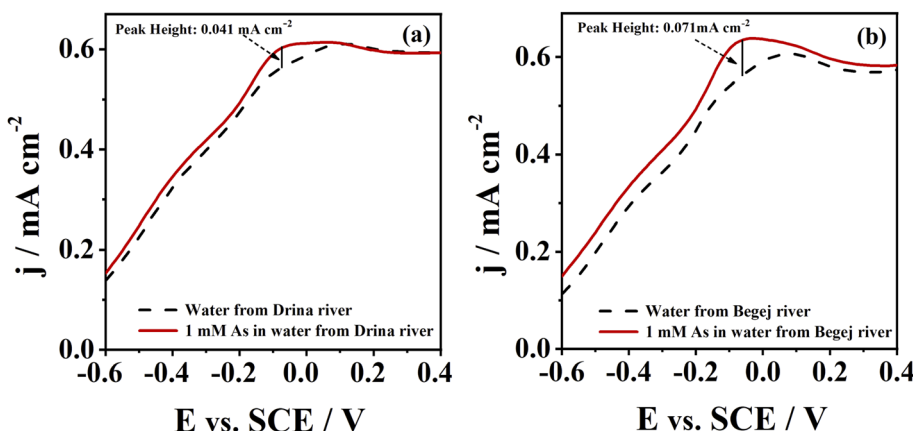


Fig. 7 Voltammograms of CoAu electrode in (a) river Drina and (b) river Begej in the absence (—) and in the presence (—) of As(III) (1 mM) recorded at a scan rate of 50 mV s^{-1} after holding the potential at -0.7 V for 60 s.

violet film in pH 7 PBS (linear range 259.82–2598.2 ppb) by differential pulse voltammetry under the optimized conditions.⁴⁷ Also, the obtained LOD value for CoAu electrode is lower

than the LOD value for Au-Sm alloy (2.3 ppb) tested in the same buffer at pH 9.2 by the ASV.⁶ On the other hand, a lower LOD of 0.13 ppb was achieved employing a carbon paste electrode

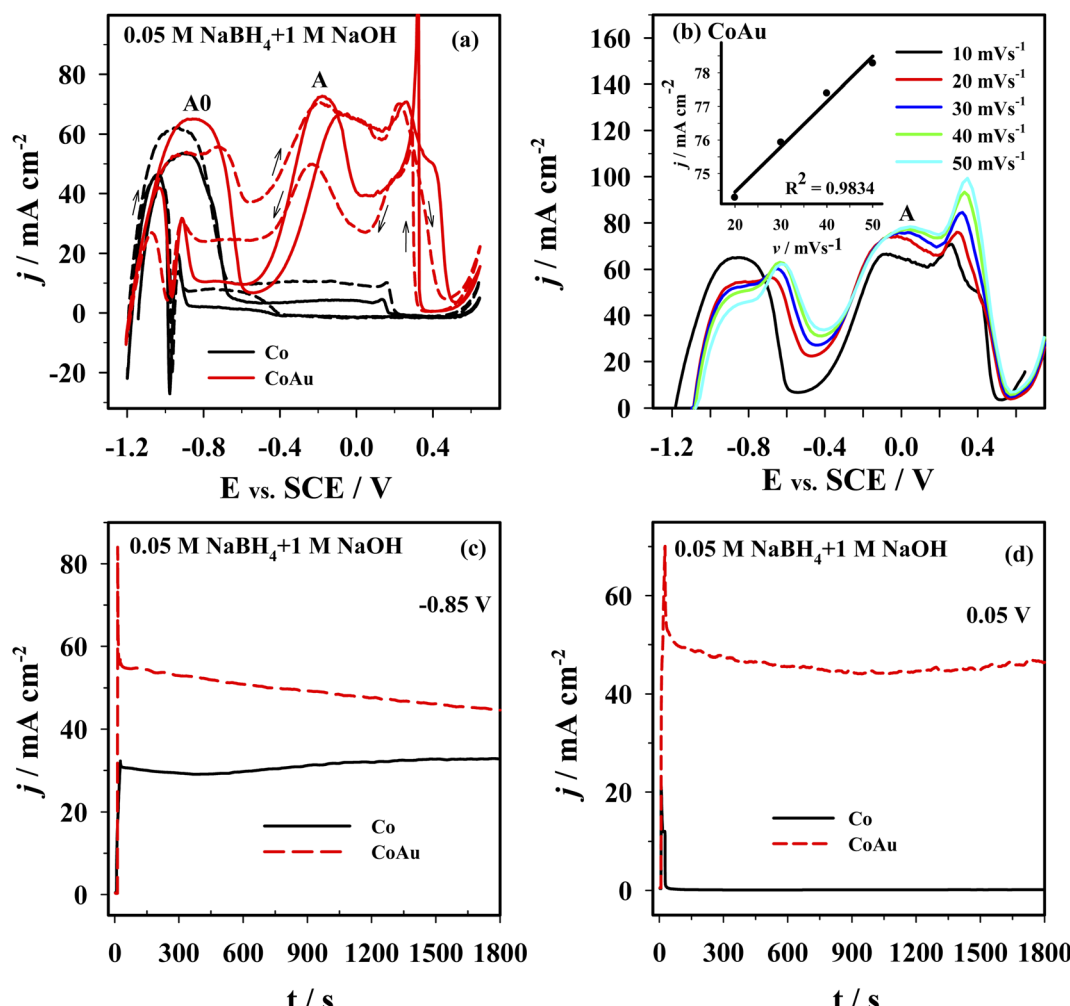
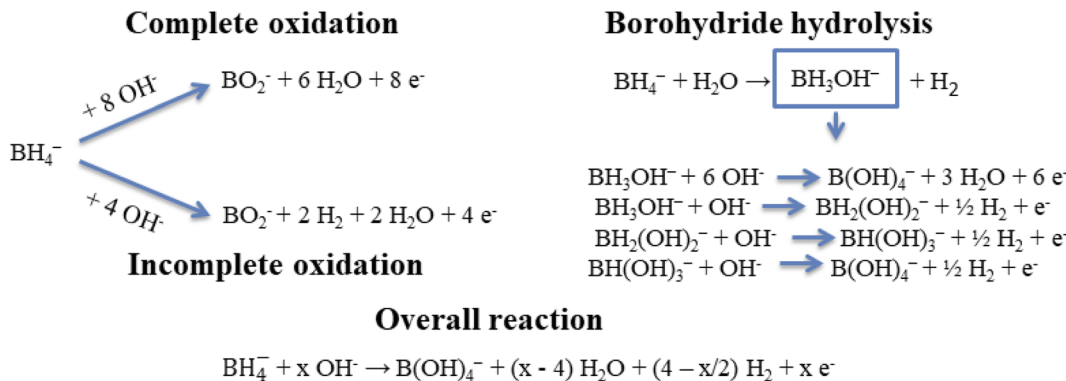


Fig. 8 (a) CVs of Co (black line) and CoAu (red line) electrodes at a scan rate of 10 mV s^{-1} : 1st cycle (solid line) and the 5th cycle (dashed line). (b) Positive-going potential scans for the Co and CoAu electrodes at different scan rates. (c and d) Chronoamperometric data of Co and AuCo electrodes at a potential of -0.85 V (vs. SCE) and 0.05 V (vs. SCE). All measurements were done in $0.05 \text{ M NaBH}_4 + 1 \text{ M NaOH}$ at 25°C .



Scheme 3 Schematic representation of the oxidation of BH_4^- ions and their hydrolysis.

modified with Au NPs – reduced graphene oxide composite in a 0.1 M phosphate buffer (pH 7.2).⁴⁸ Square-wave ASV response of nanocomposite of $\alpha\text{-MnO}_2$ with Au NPs led to a low LOD of 0.019 ppb at pH 9.0 $\text{Na}_2\text{CO}_3\text{-NaHCO}_3$ buffer solution (0.1 M), while at pH 5 a higher LOD was obtained for the same electrode.⁴⁹ MnO_x with Au NPs fabricated for the detection As(III) in alkaline media (0.1 M $\text{Na}_2\text{CO}_3\text{-NaHCO}_3$, pH 10.0) gave a low LOD of 0.057 ppb for As(III) sensing.⁵⁰

Real samples, such as river water and tap water, can contain various ions including Na^+ , K^+ , Mg^{2+} , Cu^{2+} , Sb^{3+} , NO_3^- , F^- , Cl^- , with Cu^{2+} being the main interfering metal ions during arsenic detection.⁵¹ The peak of Cu^{2+} oxidation appears at a slightly more positive potential compared to the peak of As(III) oxidation.⁵¹ Therefore, CoAu electrode response to As(III) (1 mM) was examined in presence of Cu^{2+} as model interferente. The voltammogram of the herein examined electrode showed the presence of two oxidation peaks (Fig. 6b) indicating that As(III) response is not affected by the presence of Cu^{2+} cation in $\text{NaHCO}_3 + \text{Na}_2\text{CO}_3$ buffer. The first peak at *ca.* -0.3 V corresponds to As oxidation and the second peak at *ca.* -0.04 V is related to Cu oxidation.⁵²

The potential application of CoAu electrode for arsenic detection in a real water sample was assessed and CoAu electrode showed activity for As(III) sensing in two river samples, Fig. 7. The peak corresponding to As(0) oxidation was observed in the diluted samples (without any pretreatment) at *ca.* -0.1 V. Peak current of river Drina sample reached 0.041 mA cm^{-2} while peak current of river Begej sample reached 0.071 mA cm^{-2} .

3.3. Borohydride oxidation reaction studies

The electrochemical behavior of the Co and CoAu electrodes towards the oxidation of BH_4^- ions was evaluated in an alkaline medium using cyclic voltammetry. Fig. 8a presents CVs of the Co and CoAu electrodes in a 1 M NaOH solution containing 0.05 M NaBH_4 at 25 °C. Two anodic peaks: A0 (in the low-potential region from -1.2 to -0.6 V) and A (in the potential region from -0.5 to 0 V) were seen on the anodic scans for the Co and CoAu electrodes. The first peak (A0) was attributed to the oxidation of hydrogen, generated by the catalytic hydrolysis of BH_4^- (eqn (2)) as well as to the oxidation of BH_4^- ions (eqn (1)), while the second peak (A) was attributed to the direct oxidation

of BH_4^- ions. The mechanism of the mentioned reactions is rather complicated due to the formation of intermediates, adsorption phenomenon, and influence of the electrode potential, *e.g.*, formation, adsorption, and oxidation of H_2 and BH_3OH^- , Scheme 3.⁵³⁻⁵⁸ It can be noted that during the cycling,

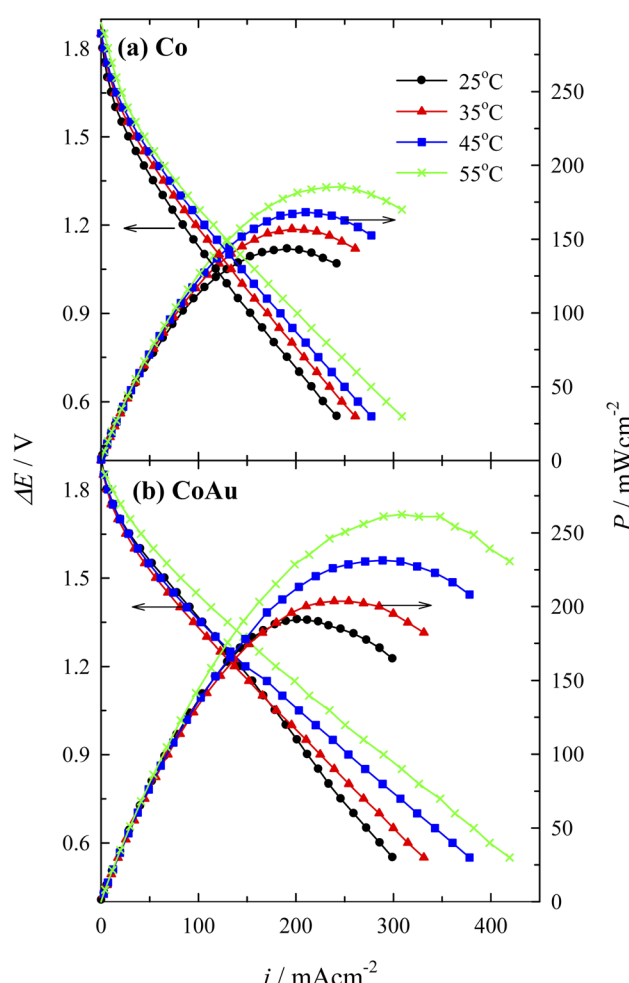


Fig. 9 Cell polarization and power density curves for the DBHPFC using (a) Co and (b) CoAu anode at operating temperatures ranging from 25 to 55 °C.



Table 3 Comparison of the parameters of the DBHPFC employing Co and CoAu anodes with DBHPFCs employing Co- and Au-based anodes reported in the literature

Electrode	T (°C)	Anolyte	Catholyte	Cell voltage at peak power density (V)	Current density at a peak power density (mA cm ⁻²)	Peak power density (mW cm ⁻²)	Ref.
Co	25	1 M NaBH ₄ + 4 M NaOH	5 M H ₂ O ₂ + 1.5 M HCl	0.75	191.19	143.47	This work
	35	1 M NaBH ₄ + 4 M NaOH	5 M H ₂ O ₂ + 1.5 M HCl	0.80	195.88	156.78	This work
	45	1 M NaBH ₄ + 4 M NaOH	5 M H ₂ O ₂ + 1.5 M HCl	0.80	210.10	168.19	This work
	55	1 M NaBH ₄ + 4 M NaOH	5 M H ₂ O ₂ + 1.5 M HCl	0.75	247.12	185.46	This work
CoAu	25	1 M NaBH ₄ + 4 M NaOH	5 M H ₂ O ₂ + 1.5 M HCl	0.95	201.19	191.25	This work
	35	1 M NaBH ₄ + 4 M NaOH	5 M H ₂ O ₂ + 1.5 M HCl	0.80	254.31	203.56	This work
	45	1 M NaBH ₄ + 4 M NaOH	5 M H ₂ O ₂ + 1.5 M HCl	0.80	288.99	231.34	This work
	55	1 M NaBH ₄ + 4 M NaOH	5 M H ₂ O ₂ + 1.5 M HCl	0.85	308.68	262.60	This work
CoAu/rGO foam	30	2 M NaOH + 0.5 M NaBH ₄	2 M H ₂ SO ₄ + 0.8 M H ₂ O ₂	0.86	150	129	60
CoAu/Ni foam	30	2 M NaOH + 0.5 M NaBH ₄	2 M H ₂ SO ₄ + 0.8 M H ₂ O ₂	0.95	85	80.5	60
Coni-NSi/Ni foam	30	0.5 M NaBH ₄ + 4 M NaOH	0.8 M H ₂ O ₂ + 2 M H ₂ SO ₄	0.96	84	80.6	61
Coni-NSi/rGO foam	30	0.5 M NaBH ₄ + 4 M NaOH	0.8 M H ₂ O ₂ + 2 M H ₂ SO ₄	0.95	95.7	91.3	61
Co/C	25	1 M NaBH ₄ + 3 M NaOH	2 M H ₂ O ₂ + 0.5 M H ₂ SO ₄	1.05	45	47.5	28
Co/TiO ₂ -NTs	25	1 M NaBH ₄ + 4 M NaOH	5 M H ₂ O ₂ + 1.5 M HCl	0.80	108.7	87	62
Au-Y	25	1 M NaBH ₄ + 4 M NaOH	5 M H ₂ O ₂ + 1.5 M HCl	0.5	295	150	28
	45	1 M NaBH ₄ + 4 M NaOH	5 M H ₂ O ₂ + 1.5 M HCl	0.6	390	215	28
Au-Ni		0.5 M NaBH ₄ + 2 M NaOH	4.5 M H ₂ O ₂ + 2 M HCl	0.57	130	74	63
Au ₅₀ Fe ₅₀ /C	25	1 M NaBH ₄ + 3 M NaOH	2 M H ₂ O ₂ + 0.5 M H ₂ SO ₄	0.50	69.6	34.9	64
Au ₆₇ Fe ₃₃ /C	25	1 M NaBH ₄ + 3 M NaOH	2 M H ₂ O ₂ + 0.5 M H ₂ SO ₄	0.51	64.8	32.9	64
Au/C	25	1 M NaBH ₄ + 3 M NaOH	2 M H ₂ O ₂ + 0.5 M H ₂ SO ₄	0.55	40.0	21.8	64
Au ₄₉ Pd ₅₁ /MWCNTs	35	5 wt% NaBH ₄ , 10 wt% NaOH, and 85 wt% H ₂ O	20 wt% H ₂ O ₂ , 5 wt% H ₃ PO ₄ , and 75 wt% H ₂ O	—	—	191.1	65
	52	5 wt% NaBH ₄ , 10 wt% NaOH, and 85 wt% H ₂ O	20 wt% H ₂ O ₂ , 5 wt% H ₃ PO ₄ , and 75 wt% H ₂ O	—	—	279.5	65
Au ₇₄ Pd ₂₆ /MWCNTs	35	5 wt% NaBH ₄ , 10 wt% NaOH, and 85 wt% H ₂ O	20 wt% H ₂ O ₂ , 5 wt% H ₃ PO ₄ , and 75 wt% H ₂ O	—	—	149.1	65
Au/CNT-G	25	2 M NaBH ₄ + 6 M NaOH	2 M H ₂ O ₂ + 1 M HCl	—	—	97	66
	40	2 M NaBH ₄ + 6 M NaOH	2 M H ₂ O ₂ + 1 M HCl	—	—	106	66
	50	2 M NaBH ₄ + 6 M NaOH	2 M H ₂ O ₂ + 1 M HCl	—	—	125	66
Au ₄₅ Co ₅₅ /C	25	1 M NaBH ₄ + 3 M NaOH	2 M H ₂ O ₂ + 0.5 M H ₂ SO ₄	0.78	85	66.50	29

current densities due to BH_4^- ions oxidation are somewhat increased and stabilized. The current density of peak A (*ca.* -0.2 V) was *ca.* 7 times higher when using CoAu electrode than using Co electrode.

Fig. 8b presents positive-going potential scans of the CoAu electrode in the NaBH_4 solution at 25°C at different scan rates with a linear regression of peak current density *vs.* scan rate. The observed shift of peak potential to positive values with the increasing scan rate is typical for irreversible processes.⁵⁹ Furthermore, BOR studies done in NaBH_4 solutions of different concentrations (0.01–0.04 M range) revealed a linear increase of the current density of peak A with the increase of concentration along with a slight shift of peak potential. These results suggest that BOR proceeds as irreversible oxidation of a bulk species under mixed kinetic and diffusion control.

Fig. 8c and d shows the chronoamperometric curves recorded using Co and CoAu electrodes in NaBH_4 solution at a fixed potential value of 0.85 V (Fig. 8c) and 0.05 V (Fig. 8d). At the end of the experimental period ($t = 30$ min), the current density values of the CoAu electrode are higher than those of Co electrode, indicating a higher electrocatalytic activity and stability of the prepared CoAu electrode towards the oxidation of BH_4^- . Namely, current densities at -0.85 V are about 1.4 and at 0.05 V are more than 300 times higher using CoAu electrode than using Co electrode (this ratio of current densities is in agreement with the voltammetry data). Furthermore, this initial 30 min i - t measurements demonstrated high stability of the prepared CoAu electrode. Thus comparison of the current density recorded at a potential of 0.05 V after 1 min and at the end of the experiment (after 30 min) revealed a decrease of only $\sim 8\%$. Comparison of current densities recorded at the same potential after 5 min and at the end of the experiment (after 30 min) showed a decrease as low as $\sim 1.3\%$.

Fuel cell measurements were performed using a homemade DBHPFC at 25 , 35 , 45 , and 55°C . During the cell discharge process, small bubbles of hydrogen and oxygen were observed at the electrodes' surface due to the chemical decomposition of BH_4^- and H_2O_2 at the anode and at the cathode, respectively. Fig. 9 presents the fuel cell polarization curves and the corresponding power density curves *versus* the current density by employing the Co (Fig. 9a) and the CoAu (Fig. 9b) as an anode. The fuel cell displayed an open circuit voltage of *ca.* 1.9 V in both cases. However, it was found that power density is significantly higher in the case of the investigated CoAu anode when compared to that of Co anode (Fig. 9). Thus, peak power densities of 143 and 191 mW cm^{-2} were attained at 25°C for DBHPFC with the Co and CoAu anode at a current density of 191 and 201 mA cm^{-2} and cell voltage of 0.75 and 0.95 V, respectively (Table 3). The peak power density increased 1.3 and 1.4 times with an increase in temperature from 25°C to 55°C using Co and CoAu anode, respectively.

Furthermore, the peak power density reached by the DBHPFC with CoAu anode is higher than that of DBHPFC with CoAu/rGO foam anode (129 mW cm^{-2} at 30°C) and CoAu/Ni foam (80.5 mW cm^{-2} at 30°C), Table 3.⁶⁰ Similarly, a peak power density of DBHPFC with CoAu anode is higher than, for instance, that of a DBHPFC operating with Au–Y anode (150

mW cm^{-2} at 25°C).²⁸ Duan and co-workers reported that DBHPFC with Au–Ni anode catalyst showed a maximum power density of 74 mW cm^{-2} at 130 mA cm^{-2} .⁶³ Improved electrode kinetics for direct oxidation of BH_4^- was reported for Au–Fe bimetallic catalysts (power density 34.9 mW cm^{-2}) in comparison to the pure Au electrode (21.8 mW cm^{-2}),⁶⁴ but still lower than kinetics/power density reached herein.

4. Conclusions

Low Au-content CoAu 3D structured electrodes were prepared by simple electroless deposition and investigated for environmental applications. Thus, a detailed study on the electrochemical behaviour of CoAu electrode in the presence of As(III) was performed. A peak corresponding to the oxidation of As(0) to As(III) could be observed at *ca.* -0.36 V in a weakly alkaline medium, with a current density double that obtained using an Au electrode. The LOD of As(III) sensing using CoAu electrode of 2.16 ppb was achieved under the optimized condition (deposition potential of -0.7 V, deposition time of 60 s) which is 5 times lower than the allowed WHO limit for arsenic in water. Furthermore, the presence of Cu(II) as a model interferent did not affect the electrode's response to As(III) presence. Finally, the analytical application of the prepared electrode toward the detection of As(III) in real water samples was proven to be successful.

DBHPFC with CoAu anode attained a peak power density of 191 mW cm^{-2} at 25°C at a cell voltage of 0.95 V, and it further increased 1.4 times with an increase in temperature to 55°C .

Hence, the CoAu electrode could be used for various environmental applications, including the detection of trace amounts of As(III) as well as BH_4^- oxidation in DBHPFCs.

Conflicts of interest

There are no conflicts to declare.

Acknowledgements

This research is funded by the European Social Fund under Measure No. 09.3.3-LMT-K-712-19-0138 'Development of Competences of Scientists, other Researchers and Students through Practical Research Activities'.

References

- 1 C. Li, O. J. H. Chai, Q. Yao, Z. Liu, L. Wang, H. Wang and J. Xie, *Mater. Horiz.*, 2021, **8**, 1657–1682.
- 2 L. Bu, Q. Xie and H. Ming, *J. Alloys Compd.*, 2020, **823**, 153723.
- 3 J. Milikić, U. Stamenović, V. Vodnik, S. P. Ahrenkiel and B. Šljukić, *Electrochim. Acta*, 2019, **328**, 135115.
- 4 D. Zhang, K. Ye, J. Yin, K. Cheng, D. Cao and G. Wang, *New J. Chem.*, 2014, **38**, 5376–5381.
- 5 H. Zhang, G. Xu, L. Zhang, W. Wang, W. Miao, K. Chen, L. Cheng, Y. Li and S. Han, *Renew. Energy*, 2020, **162**, 345–354.

6 K. Radinović, J. Milikić, D. M. F. Santos, A. Saccone, S. De Negri and B. Šljukić, *J. Electroanal. Chem.*, 2020, **872**, 114232.

7 K. Radinović, J. Milikić, V. Vodnik, M. Otoni and B. Šljukić, *Synth. Methods*, 2021, **278**, 116834.

8 L. Wang, X. Peng, H. Fu, C. Huang, Y. Li and Z. Liu, *Biosens. Bioelectron.*, 2020, **147**, 111777.

9 D. Banik, S. Kumar and A. Kumar, *Spectrochim. Acta, Part A*, 2021, **246**, 119047.

10 K. Mao, H. Zhang, Z. Wang, H. Cao, K. Zhang, X. Li and Z. Yang, *Biosens. Bioelectron.*, 2020, **148**, 111785.

11 X. Xu, X. Niu, X. Li, Z. Li, D. Du and Y. Lin, *Sens. Actuators, B*, 2020, **315**, 128100.

12 S. Sikdar and M. Kundu, *ChemBioEng Rev.*, 2018, **5**, 18–29.

13 X. Yu, C. Liu and Y. Guo, *Molecules*, 2019, **24**, 926.

14 S. Li, C. Zhang, S. Wang, Q. Liu and H. Feng, *Analyst*, 2018, **143**, 4230–4246.

15 K. Pungjunun, S. Chaiyo, I. Jantrahong, S. Nantaphol, W. Siangproh and O. Chailapakul, *Microchim. Acta*, 2018, **185**, 324.

16 B. K. Bansod, T. Kumar, S. Rana and I. Singh, *Biosens. Bioelectron.*, 2017, **94**, 443–455.

17 M. Yang, Z. Guo, L. N. Li, Y. Y. Huang, J. H. Liu, Q. Zhou, X. Chen and X. J. Huang, *Sens. Actuators, B*, 2016, **231**, 70–78.

18 A. Salimi, H. Mamkhezri, R. Hallaj and S. Soltanian, *Sens. Actuators, B*, 2008, **129**, 246–254.

19 V. A. Online and G. Lota, *RSC Adv.*, 2021, **11**, 15639–15655.

20 C. P. de Leon, F. C. Walsh, D. Pletcher, D. J. Browning and J. B. Lakeman, *J. Power Sources*, 2006, **155**, 172–181.

21 J. Ma, N. A. Choudhury and Y. Sahai, *Renew. Sustain. Energy Rev.*, 2010, **14**, 183–199.

22 M. Martins, J. Milikić, B. Šljukić, G. S. P. Soylu, B. Yurtcan, G. Bozkurt and D. M. F. Santos, *Microporous Mesoporous Mater.*, 2019, **273**, 286–293.

23 X. Geng, H. Zhang, Y. Ma and H. Zhong, *J. Power Sources*, 2010, **195**, 1583–1588.

24 M. Chatenet and J. Diard, *Electrochim. Acta*, 2009, **54**, 1687–1693.

25 M. Chatenet, F. Micoud, I. Roche, E. Chainet and J. Vondrák, *Electrochim. Acta*, 2006, **51**, 5452–5458.

26 F. H. B. Lima, A. M. Pasqualetti, M. B. Molina, M. Chatenet and E. A. Ticianelli, *Electrochim. Acta*, 2012, **84**, 202–212.

27 D. V. Bavykin and F. C. Walsh, *Electrochim. Commun.*, 2006, **8**, 1655–1660.

28 G. Backović, J. Milikić, S. De Negri, A. Saccone, B. Šljukić and D. M. F. Santos, *J. Alloys Compd.*, 2021, **857**, 158273.

29 F. Pei, Y. Wang, X. X. Wang, P. He, Q. Chen, X. X. Wang, H. Wang, L. Yi and J. Guo, *Int. J. Hydrogen Energy*, 2010, **35**, 8136–8142.

30 P. He, X. Wang, P. Fu, H. Wang and L. Yi, *Int. J. Hydrogen Energy*, 2011, **36**, 8857–8863.

31 X. Dai, O. Nekraseova, M. E. Hyde and R. G. Compton, *Anal. Chem.*, 2004, **76**, 5924–5929.

32 X. Liu, Y. Yao, Y. Ying and J. Ping, *TrAC, Trends Anal. Chem.*, 2019, **115**, 187–202.

33 P. Giannozzi, S. Baroni, N. Bonini, M. Calandra, R. Car, C. Cavazzoni, D. Ceresoli, G. L. Chiarotti, M. Cococcioni, I. Dabo, A. Dal Corso, S. De Gironcoli, S. Fabris, G. Fratesi, R. Gebauer, U. Gerstmann, C. Gouguassis, A. Kokalj, M. Lazzeri, L. Martin-Samos, N. Marzari, F. Mauri, R. Mazzarello, S. Paolini, A. Pasquarello, L. Paulatto, C. Sbraccia, S. Scandolo, G. Scelauzero, A. P. Seitsonen, A. Smogunov, P. Umari and R. M. Wentzcovitch, *J. Phys. Condens. Matter*, 2009, **21**, 395502.

34 J. P. Perdew, K. Burke and M. Ernzerhof, *Phys. Rev. Lett.*, 1996, **77**, 3865–3868.

35 D. Joubert, *Phys. Rev. B: Condens. Matter Mater. Phys.*, 1999, **59**, 1758–1775.

36 R. Tarozaite, A. Sudavičius, Z. Sukackiene and E. Norkus, *Trans. Inst. Met. Finish.*, 2014, **92**, 146–152.

37 V. da R. Caffarena, J. L. Capitaneo, R. A. Simão and A. P. Guimarães, *Mater. Res.*, 2006, **9**, 205–208.

38 A. Alshareef, K. Laird and R. B. M. Cross, *Acta Metall. Sin. (English Lett.)*, 2017, **30**, 29–35.

39 S. Elzey, J. Baltrusaitis, S. Bian and V. H. Grassian, *J. Mater. Chem.*, 2011, **21**, 3162–3169.

40 S. Hebié, K. B. Kokoh, K. Servat and T. W. Napporn, *Gold Bull.*, 2013, **46**, 311–318.

41 A. Lu, D. Peng, F. Chang, Z. Skeete, S. Shan, A. Sharma, J. Luo and C. Zhong, *ACS Appl. Mater. Interfaces*, 2016, **8**, 20082–20091.

42 C. Zhou, M. Yang, S. S. Li, T. J. Jiang, J. H. Liu, X. J. Huang and X. Chen, *Electrochim. Acta*, 2017, **231**, 238–246.

43 V. Poza-Nogueiras, M. Pazos, M. Á. Sanromán and E. González-Romero, *Electrochim. Acta*, 2019, **320**, 1–13.

44 A. Karthika, S. Selvarajan, P. Karuppasamy, A. Suganthi and M. Rajarajan, *J. Phys. Chem. Solids*, 2019, **127**, 11–18.

45 J. Milikić, I. Stoševski, J. Krstić, Z. Kačarević-Popović, Š. Miljanić and B. Šljukić, *J. Anal. Methods Chem.*, 2017, **2017**, 1–9.

46 A. O. Idris, J. P. Mafa, N. Mabuba and O. A. Arotiba, *Russ. J. Electrochem.*, 2017, **53**, 170–177.

47 M. Rajkumar, S. Thiagarajan and S. M. Chen, *Int. J. Electrochem. Sci.*, 2011, **6**, 3164–3177.

48 S. Sahoo, P. K. Sahoo and A. K. Satpati, *Electroanalysis*, 2017, **29**, 1400–1409.

49 M. Yang, X. Chen, T. J. Jiang, Z. Guo, J. H. Liu and X. J. Huang, *Anal. Chem.*, 2016, **88**, 9720–9728.

50 S. Wu, Q. Zhao, L. Zhou and Z. Zhang, *Electroanalysis*, 2014, **26**, 1840–1849.

51 P. Carrera, P. J. Espinoza-Montero, L. Fernández, H. Romero and J. Alvarado, *Talanta*, 2017, **166**, 198–206.

52 C. Sullivan, D. Lu, E. Brack, C. Drew and P. Kurup, *Anal. Chim. Acta*, 2020, **1107**, 63–73.

53 D. Alligier, E. Petit and U. B. Demirci, *Int. J. Hydrogen Energy*, 2022, **47**, 23310–23315.

54 K. K. Das, L. Paramanik and K. Parida, *Int. J. Hydrogen Energy*, 2021, **46**, 24484–24500.

55 J. Milikić, R. C. P. Oliveira, I. Stoševski, J. Krstić, R. Hercigonja, Š. Miljanić, D. M. F. Santos and B. Šljukić, *New J. Chem.*, 2019, **43**, 14270–14280.

56 B. Hu, C. Xu, P. Chen, J. Yu, B. Hu, Q. Xiang, Y. Cen, Y. Liu, D. Yu and C. Chen, *Int. J. Hydrogen Energy*, 2021, **46**, 27516–27528.



57 Y. E. Duan, S. Li, Q. Tan, Y. Chen, K. Zou, X. Dai, M. Bayati, B. B. Xu, L. Dala and T. X. Liu, *Int. J. Hydrogen Energy*, 2021, **46**, 15471–15481.

58 A. M. A. Elsheikh, G. Backović, R. C. P. Oliveira, C. A. C. Sequeira, J. Mc Gregor and B. Šljukić, *Nanomaterials*, 2021, **11**, 1441.

59 A. J. Bard and L. R. Faulkner, *Electrochemical Methods: Fundamentals and Applications*, 2nd edn, 2000.

60 B. Li, C. Song, D. Zhang, K. Ye, K. Cheng, K. Zhu, J. Yan, D. Cao and G. Wang, *Carbon*, 2019, **152**, 77–88.

61 B. Li, Q. Yan, C. Song, P. Yan, K. Ye, K. Cheng, K. Zhu, J. Yan, D. Cao and G. Wang, *Appl. Surf. Sci.*, 2019, **491**, 659–669.

62 A. Balčiūnaitė, L. Tamašauskaitė-Tamašiūnaitė, D. M. F. Santos, A. Zabielaite, A. Jagminienė, I. Stankevičienė and E. Norkus, *Fuel Cells*, 2017, **17**, 690–697.

63 D. Duan, J. Liang, H. Liu, X. You, H. Wei, G. Wei and S. Liu, *Int. J. Hydrogen Energy*, 2015, **40**, 488–500.

64 L. Yi, W. Wei, C. Zhao, L. Tian, J. Liu and X. Wang, *J. Power Sources*, 2015, **285**, 325–333.

65 T. H. Oh, *Renew. Energy*, 2021, **163**, 930–938.

66 A. Uzundurukan, E. S. Akça, Y. Budak and Y. Devrim, *Renew. Energy*, 2021, **172**, 1351–1364.

